https://doi.org/10.53964/jmn.2026001

https://www.innovationforever.com

Journal of Modern Nanotechnology

ISSN 2788-8118 (Online)

Open Access

Research Article

Boosting Furnace Efficiency with Nanofluids

Mohammad YaghoubAbdollahzadeh Jamalabadi[1*]

[1]Faculty of Marine Engineering, Chabahar Maritime University, Chabahar, Iran

[*]**Correspondence to: Mohammad YaghoubAbdollahzadeh Jamalabadi,** Faculty of Marine Engineering, Chabahar Maritime University, Chabahar 99717-56499, Iran; Email: my.abdollahzadeh@cmu.ac.ir

Received: October 24, 2025 **Revised:** December 15, 2025 **Accepted:** March 9, 2026 **Published:** April 21, 2026

Abstract

Objective: The Bridgman–Stockbarger method is a critical technique for producing high-purity single crystals, with significant applications in semiconductor and photovoltaic industries. This study explores the enhancement of thermal performance in coaxial cylindrical furnaces—common in crystal growth systems—through the use of nanofluids.

Methods: A Multi-Relaxation-Time lattice Boltzmann method (MRT-LBM) is employed to simulate natural convection and heat transfer within the annular space between vertical cylinders. The model incorporates radial coordinates into the temperature distribution, simplifying the source term requirement. Validation via Chapman–Enskog analysis confirms the recovery of the macroscopic energy equation.

Results: Results include detailed distributions of temperature, velocity streamlines, and entropy generation, highlighting improvements in heat transfer efficiency and thermodynamic performance.

Conclusion: This research underscores the potential of nanofluid-based thermal management to support energy-efficient material processing, with direct implications for the development of advanced materials, including high-performance ceramics, composites, and sustainable construction technologies.

Keywords: Bridgman–Stockbarger method, natural convection, thermal management, nanofluids, lattice Boltzmann method, entropy generation; sustainable materials, building material science, energy efficiency

Citation: Jamalabadi MY. Boosting Furnace Efficiency with Nanofluids. *J Mod Nanotechnol*, 2026; 6: 1. DOI: 10.53964/jmn.2026001.

1 INTRODUCTION

Industrial crystal growth processes represent a significant environmental challenge in modern manufacturing, consuming substantial energy resources while generating considerable thermal waste. The semiconductor and photovoltaic industries, which rely heavily on high-purity crystal production through methods such as Bridgman–Stockbarger technique, contribute to approximately 2-3% of global industrial energy consumption. Traditional crystal growth furnaces operate at temperatures exceeding 1,000°C for extended periods, requiring precise thermal control that typically involves energy-intensive heating and cooling cycles. This energy demand not only increases operational costs but also contributes to greenhouse gas emissions and environmental degradation. Furthermore, thermal inefficiencies in these processes often result in crystal

defects, leading to material waste and increased resource consumption as defective products must be reprocessed or discarded.

The Bridgman–Stockbarger method, is used a temperature gradient and a moving crucible for growing boules (single-crystal ingots such as tungsten, antimony, bismuth, tellurium, cadmium, zinc, and tin), and solidifying polycrystalline ingots. Bridgman[1] explores the physical properties of various single crystals, including tungsten, antimony, bismuth, tellurium, cadmium, zinc, and tin. First heating polycrystalline material above its melting point and then slowly cooling it from one end of its container. The polycrystalline ingots can be produced from a feedstock consisting of rods, chunks, or any irregularly shaped pieces once they are melted and allowed to re-solidify. The resultant microstructure of the ingots so obtained is characteristic of directionally solidified metals and alloys with their aligned grains. Stockbarger[2] focuses on the production of large single crystals of lithium fluoride, which is important for various applications in materials science.

The integration of sustainable technologies into energy-intensive manufacturing processes has become a critical component of environmental resource management and climate change mitigation strategies. Nanotechnology applications in thermal management systems offer promising pathways for reducing the environmental footprint of industrial processes while maintaining product quality standards. Enhanced heat transfer mechanisms through nanofluid implementation can significantly improve thermal uniformity and reduce energy consumption in high-temperature applications. This approach aligns with sustainable development goals by optimizing resource utilization, minimizing waste generation, and reducing the overall environmental impact of precision manufacturing. The development of energy-efficient crystal growth technologies represents a crucial intersection between advanced materials science and environmental engineering, where improved thermal management directly translates to reduced energy consumption and decreased environmental burden.

Nanofluids are important in many aspects of science and technology. For example, in medicine, nanoparticles can be used to deliver drugs directly to specific cells in the body, making treatments more effective and reducing side effects. In electronics, nanoparticles can be used to enhance the performance of devices by improving conductivity and energy efficiency. They can also be used in environmental science to remove pollutants from water and air. Since for decades the modelling of ensemble average properties of nanoparticles are important for scientists. Broadbent[3] explores the theory of Brownian movement, providing valuable insights into the behavior of particles suspended in a fluid. as well Understanding thermal conductivity is crucial for various engineering and materials science applications. Hamilton and Crosser[4] investigated the thermal conductivity of heterogeneous systems composed of two different components. Their model improved by Levin and Miller[5] by Maxwell's theory which is a fundamental property calculation in the field of electromagnetism.

There have been numerous studies conducted to simulate the flow of fluids and the transfer of heat during natural convection in enclosures. These research projects have found applications in a wide range of scientific fields, such as meteorology, thermal storage, solar collectors, passive cooling, cooling electronic devices, ventilation, and the drying process[6-9]. Kumar and Kalam[6] investigated the heat transfer characteristics and flow behavior in vertical cylindrical annuli. They compared cases where the inner wall was hotter than the outer wall and cases where the horizontal walls were perfectly conducting. They used numerical methods to calculate heat transfer rates and flow fields for different ranges of parameters. They also noticed some differences between the numerical and experimental data and came up with new correlations for heat transfer rates. Crawford and Lemlich[7] focuses on natural convection in an annulus between two rotating vertical cylinders. It examines the heat transfer and fluid flow characteristics in this system. Yu and Choi[8] studied the role of interfacial layers in enhancing the thermal conductivity of nanofluids. They propose a modified Hamilton-Crosser model to better understand the thermal behavior of nanofluids. Li et al.[9] presents a lattice Boltzmann model for simulating axisymmetric thermal flows. They provide insights into the behavior of heat transfer in systems with axisymmetric geometries. They developed a lattice Boltzmann model called the multiple-relaxation-time (MRT) model to simulate the axisymmetric convection-diffusion equation in a cylindrical coordinate system. They rearranged the equation to work in a Cartesian coordinate system and included additional terms as sources. The model directly calculates the gradient of the scalar quantity, eliminating the need for finite-difference calculations. They conducted various numerical tests to validate the model's accuracy, including convection-diffusion in an annulus, heat conduction in a sphere, and natural convection in a cylindrical annulus. The results showed good agreement with analytical solutions and published results.

Adding nanoparticles to the air can pose potential dangers. These tiny particles, due to their small size, can easily enter our respiratory system and reach deep into our lungs. They have the potential to cause inflammation, oxidative stress, and damage to lung tissue. Additionally, certain nanoparticles may have toxic properties that can further contribute to health risks. It is important to understand and mitigate these dangers to ensure the safety of individuals working with or exposed

to nanoparticles in the air. Proper ventilation systems and protective measures are crucial in minimizing the potential harm associated with airborne nanoparticles. Since the strategies are employed to control exposure to Titanium Dioxide, Carbon Nanotubes, Nanofibers, and carbonaceous nanomaterials in the industry and provides relevant information and guidance[10]. Based on the NIOSH RELs for nanoparticles, the Occupational Safety and Health Administration (OSHA), in reference 2 announced their recommended exposure limit of 1μg/m^3 for carbon nanotubes and carbon nanofibers and 0.3mg/m^3[11] for nanoscale particles of TiO_2. By contrast, the NIOSH REL for fine TiO_2 is 2.4mg/m^3[12].

Li et al.[13] came up with a thermal lattice Boltzmann model specifically for axisymmetric thermal flows. This model is based on the double-distribution-function lattice Boltzmann method, which is known for its numerical stability. this model is simpler compared to existing axisymmetric thermal lattice Boltzmann models, while still maintaining the key features of the standard lattice Boltzmann method. They tested the model by simulating thermally developing laminar flows in circular ducts and natural convection between two vertical cylinders. The results matched up well with analytical solutions and previous studies.

These references cover a range of topics related to the dispersion of nanoparticles, thermal lattice Boltzmann simulations, and heat transfer in nanofluids[14-19]. The study of Mehel and Murzyn[14] examines the dispersion of nanoparticles in the wake of a vehicle model under different air velocities using wind tunnel experiments. Khakrah et al.[15] study presents a thermal lattice Boltzmann simulation of natural convection in a multi-pipe sinusoidal-wall cavity filled with a nanofluid. They used a modern numerical method called hybrid lattice Boltzmann-TVD to simulate natural convection in a partially heated cavity filled with various nanofluids, using Buongiorno's model. They discovered that at low Rayleigh numbers, heat transfer continuously improves. However, at high Rayleigh numbers, there's an optimal point where heat transfer enhancement reaches its maximum. Additionally, they found that the average Nusselt number decreases as the heater length increases. During turbulent natural convection in the cavities, researchers calculated the average Nusselt number at different Prandtl and Grashof numbers. They compared the cases with and without thermal radiation. Jamalabadi[16] discusses the lattice Boltzmann simulation of film boiling in ferrofluids. The Sankar et al.[17] research found that as the Rayleigh number increases, the heat loss from the room also increases. Additionally, increasing the aspect ratio improves the thermal efficiency. It's prooving how these factors play a role in heat transfer. The study investigates the conjugate buoyant convective transport of nanofluids in an enclosed annular geometry[17]. Swamy et al.[18] research explores the conjugate heat transfer of an aqueous hybrid nanoliquid between coaxial cylinders under the influence of a magnetic field. Hayat et al.[19] compares the radiative and dissipative flow of a hybrid nanofluid between two coaxial cylinders using numerical simulations. They study the entropy generation during turbulent natural convection in a square cavity included with an internal heat generation. Alami et al.[20] paper provides a critical insight into the use of nanofluids for enhancing heat transfer as well as influence of grid and boundary conditions on the heat and mass transfer. They discovered that the flow structure and heat transfer rate of the cavity are closely related to the dimensionless length of the heater. The natural convection phenomenon has been extensively studied by researchers in enclosures with different configurations, operating fluids, initial and boundary conditions, and numerical approaches. More boundary conditions are reviewed by Capper and Rudolph[21] discussed crystal growth technology in their book. The book provides valuable information on the principles and techniques of crystal growth. Hanif et al.[22] discusses the heat transfer characteristics of a hybrid nanofluid flowing between two coaxial cylinders. In this research, the focus was on investigating the flow characteristics of hybrid nanofluids between two permeable cylinders in the presence of thermal radiation and heat generation. The numerical solutions were obtained using the finite difference method. The study examined the impact of factors such as nanoparticle fraction, porous medium, radiation, heat generation, and angular frequency on the velocity, temperature, and Nusselt number. The findings were effectively presented through the use of graphs and tables. Notably, it was observed that the TiO2/water nanofluid exhibited the maximum velocity, while the TiO2-Ag/water nanofluid displayed the highest temperature distribution. Additionally, the Nusselt number of the fluid experienced significant increases of 17.5%, 19.7%, and 21.7% upon the addition of TiO2, TiO2-Ag, and Ag nanoparticles respectively. These results shed light on the intricate relationship between the considered parameters and the flow behavior of the nanofluid system. Venkatachalappa et al.[23] investigated the impact of rotation on the flow driven by buoyancy in an annular cavity formed by two concentric vertical cylinders. The cylinders rotated at different angular velocities, while the side walls were maintained at different temperatures and the top and bottom walls were adiabatic. The researchers used numerical methods to solve the governing equations and obtained results for various parameters such as the Grashof number, rotational speeds, and Prandtl number. They found that the flow patterns and heat transfer were influenced by these parameters, with different behaviors observed for different rotational configurations. The study provides insights into the complex interaction between rotation and buoyancy-driven flow in this system.

Nanofluid also used to improved systems as investigation of nanoparticle-enhanced lubricant films in thermal design applications[24], smoothed particle hydrodynamics modeling of nano-fluid flows for forced convection heat transfer[25], and

the analysis of Brownian motion effects on phase change materials containing nanoparticles[26]. In biomedical applications, examining the toxicity and therapeutic potential of silver nanoparticles synthesized from seaweed in aquatic species[27], and exploring magnetohydrodynamic effects on nanoparticle transport for pharmaceutical applications are another examples[28]. Additionally, nanoparticle-enhanced phase change materials for cooling applications of electronic devices[29] and surface acoustic wave sensors[30] demonstrates practical engineering applications of nanotechnology[31-34].

The above references cover a range of topics in physics and materials science, providing valuable insights into single crystals, crystal production, Brownian movement, and thermal conductivity models. The objective of this research is to investigate the natural convection phenomenon in a vertical annular space filled with nanofluid. To simulate the flow and heat transfer of the nanofluid, the MRT lattice Boltzmann method is utilized. The thermo-physical properties of the nanofluid are measured using advanced devices and incorporated into the numerical simulations. The Rayleigh number, solid volume fraction of the nanofluid, and cylinders configuration are the key factors that govern the study. The pursuit of advanced and sustainable building materials has driven innovations in material processing techniques, particularly those requiring precise thermal management. The Bridgman–Stockbarger furnace, widely used for high-purity crystal growth, exemplifies a system where controlled solidification processes are critical not only for semiconductors but also for novel construction materials such as engineered ceramics, composite reinforcements, and phase-change materials for thermal regulation in buildings. However, the energy-intensive nature of these furnaces poses challenges for sustainable manufacturing. In this context, nanofluids—engineered suspensions of nanoparticles in base fluids—offer a promising pathway to enhance heat transfer efficiency, reduce energy consumption, and improve thermal uniformity. This study investigates the integration of nanofluids within the annular space of a Bridgman–Stockbarger furnace to optimize natural convection and heat transfer dynamics. By leveraging numerical simulations, we demonstrate how nanofluid-enabled thermal management can contribute to more energy-efficient material processing, aligning with the goals of sustainable building material production and supporting the development of next-generation construction technologies.

2 LATTICE BOLTZMANN EQUATION FOR AXISYMMETRIC INCOMPRESSIBLE FLOW

2.1 D2Q9 MRT Lattice Boltzmann Model for Fluid Flow

The two-dimensional axisymmetric form of the MRT lattice Boltzmann method of each particle at time and location for the time step δ_t can be defined as:

$$f(x+e_i\delta_t, t+\delta_t) - f(x,t) = -M^{-1}SM(f-f^{eq}) + \delta_t M^{-1}\left(I-\frac{S}{2}\right)F \quad (1)$$

where is the distribution function x, is the equilibrium condition, is transformation matrix, and the relaxation time matrix for D2Q9 model is $S=diag(S_0,S_1,S_2,S_3,S_4,S_5,S_6,S_7,S_8)^{-1}$. The discrete velocities, are:

$$e_i = \begin{cases} (0,0), i=0 \\ c\left(cos\left[(i-1)\frac{\pi}{2}\right], sin\left[(i-1)\frac{\pi}{2}\right]\right), i=14 \\ \sqrt{2}c\left(cos\left[(2i-1)\frac{\pi}{2}\right], sin\left[(2i-1)\frac{\pi}{2}\right]\right), i=58 \end{cases} \quad (2)$$

where represents the lattice speed, and is the lattice spacing.

The equilibrium distribution function is defined as follows:

$$f_i^{eq} = r\rho w_i\left[1+\frac{e_i.u}{c_s^2}+\frac{(e_i.u)^2}{2c_s^4}-\frac{u^2}{2c_s^2}\right] \quad (3)$$

here denotes the weight coefficient, and the magnitudes of weight coefficients are as

$$w_0 = 4/9, \text{ for and for } j = 58 \quad (4)$$

The transformation matrix is given as follows:

$$M = \begin{bmatrix} 1 & 1 & 1 & 1 & 1 & 1 & 1 & 1 & 1 \\ -4 & -1 & -1 & -1 & -1 & 2 & 2 & 2 & 2 \\ 4 & -2 & -2 & -2 & -2 & 1 & 1 & 1 & 1 \\ 0 & 1 & 0 & -1 & 0 & 1 & -1 & -1 & 1 \\ 0 & -2 & 0 & 2 & 0 & 1 & -1 & -1 & 1 \\ 0 & 0 & 1 & 0 & -1 & 1 & 1 & -1 & -1 \\ 0 & 0 & -2 & 0 & 2 & 1 & 1 & -1 & -1 \\ 0 & 1 & -1 & 1 & -1 & 0 & 0 & 0 & 0 \\ 0 & 0 & 0 & 0 & 0 & 1 & -1 & 1 & -1 \end{bmatrix} \quad (5)$$

The velocity distribution function in the velocity space is:

$$m = Mf = r(\rho, e, \varepsilon, j_x, q_x, j_r, q_r, p_{xx}, p_{xr})^T \quad (6)$$

where $f=(f_0,f_1,\ldots,f_8)^T$, shows the density, denotes the total energy, is related to energy square, and are the momentum components correspond to and r, respectively. and represent the axial and radial velocity components, respectively. and are

the energy flux components at and directions, and and show the diagonal and off-diagonal components of the stress tensor, respectively. The equilibrium velocity distribution function in the velocity space is:

$$m^{eq} = Mf^{eq} = r\begin{bmatrix} \rho \\ e^{eq} \\ \varepsilon^{eq} \\ j_x \\ q_x^{eq} \\ j_r \\ q_r^{eq} \\ p_{xx}^{eq} \\ p_{xr}^{eq} \end{bmatrix} = r\rho\begin{bmatrix} 1 \\ -2+3(u_x^2+u_r^2) \\ 1-3(u_x^2+u_r^2) \\ u_x \\ -u_x \\ u_r \\ -u_r \\ u_x^2-u_r^2 \\ u_xu_r \end{bmatrix} (7)$$

where $f^{eq} = (f_0^{eq}, f_1^{eq}, ..., f_8^{eq})^T$. The collision process is

$$Collision: \tilde{m} = m - S(m-m^{eq}) + \delta_t\left(I - \frac{S}{2}\right)F (8)$$

and streaming process are is:

$$Streaming: f_i(x+e_i\delta_t, t+\delta_t) = \tilde{f}_i(x,t) (9)$$

Where represents the Unit matrix, and denotes the post-collision distribution function, shows the post-collision distribution function in the moment space, and shows the force term in the moment space which is defined as follows[16]:

$$F = r\begin{bmatrix} 0 \\ -3\rho(u_x\tilde{a}_x + u_r\tilde{a}_r)(-2+3u_x^2+3u_r^2) \\ 3\rho(u_x\tilde{a}_x + u_r\tilde{a}_r)(-2+3u_x^2+3u_r^2) \\ \rho\tilde{a}_x \\ \rho(3\tilde{a}_xu_r^2 + 6u_xu_r\tilde{a}_r - \tilde{a}_x) \\ \rho\tilde{a}_r \\ \rho(3\tilde{a}_ru_x^2 + 6u_xu_r\tilde{a}_x - \tilde{a}_r) \\ -\rho[3(u_x\tilde{a}_x + u_r\tilde{a}_r)(u_x^2-u_r^2) - 2(u_x\tilde{a}_x - u_r\tilde{a}_r)] \\ -\rho[3u_xu_r(u_x\tilde{a}_x + u_r\tilde{a}_r) - (u_x\tilde{a}_r + u_r\tilde{a}_x)] \end{bmatrix} (10)$$

where $\tilde{a}_x = a_x$, $\tilde{a}_r = a_r + \frac{RT}{r}\left[1 + \frac{2(\tau-1/2)u_r}{r}\right]$, while is the external acceleration.

The macroscopic density and velocity are defined as follows :

$$\rho = \frac{1}{r}\sum_i f_i (11)$$

$$u_x = \frac{1}{r}\left[\sum_{i=0}^{8} e_{ix}f_i/\rho + \frac{\delta_t}{2}ra_x\right] (12)$$

$$u_r = \frac{1}{r^2+\tau\delta_tRT}\left[\sum_{i=0}^{8} e_{ir}f_i/\rho + \frac{\delta_t}{2}ra_r + \frac{\delta_t}{2}rRT\right] (13)$$

where is gas constant, and is temperature and

$$\tau = \frac{1}{s_7} = \frac{1}{s_8} (14)$$

sound speed is

$$c_s = \sqrt{RT} = c/\sqrt{3} (15)$$

As the mass conservation is:

$$\frac{\partial u_x}{\partial x} + \frac{1}{r}\frac{\partial(ru_r)}{\partial r} = 0 (16)$$

the momentum conservation in axial direction is:

$$\frac{du_x}{dt} = -\frac{1}{\rho}\frac{\partial p}{\partial x} + \nu\left[\frac{1}{r}\frac{\partial}{\partial r}\left(r\frac{\partial u_x}{\partial r}\right) + \frac{\partial^2 u_x}{\partial x^2}\right] + a_x (17)$$

and the momentum conservation in radial direction is:

$$\frac{du_r}{dt} = -\frac{1}{\rho}\frac{\partial p}{\partial r} + \nu\left[\frac{\partial}{\partial r}\left(\frac{1}{r}\frac{\partial(ru_r)}{\partial r}\right) + \frac{\partial^2 u_r}{\partial r^2}\right] + a_r (18)$$

where viscosity:

$$\nu = c_s^2\left(\tau - \frac{1}{2}\right)\delta_t (19)$$

2.2 D2Q9 MRT Lattice Boltzmann Model for Heat Transfer

The evolution function for the temperature field based on transformation matrix, is given as follows:

$$h(x+e_i\delta_t, t+\delta_t) - h(x,t) = -M^{-1}\Theta M(h-h^{eq}) + \delta_t M^{-1}\Psi (20)$$

where is the temperature distribution function, and relaxation time matrix $\Theta = diag(\sigma_0, \sigma_1, \sigma_2, \sigma_3, \sigma_4, \sigma_5, \sigma_6, \sigma_7, \sigma_8)^{-1}$. The equilibrium distribution function for the temperature is:

$$h_i^{eq} = rTw_i\left[1 + \frac{e_i.u}{c_s^2} + \frac{(e_i.u)^2}{2c_s^4} - \frac{u^2}{2c_s^2}\right] (21)$$

equilibrium moments of the distribution functions is:

$$n^{eq} = Mh^{eq} = rT\begin{bmatrix} 1 \\ -2+3(u_x^2+u_r^2) \\ 1-3(u_x^2+u_r^2) \\ u_x \\ -u_x \\ u_r \\ -u_r \\ u_x^2-u_r^2 \\ u_xu_r \end{bmatrix} (22)$$

and the source term is:

$$\Psi = (0,0,0,b_x,-b_x,b_r,-b_r,0,0)^T (23)$$

where

$$(b_x,b_r)^T = \left(0, c_s^2\left(1-\frac{\sigma_5}{2}\right)T\right)^T \Psi = (0,0,0,b_x,-b_x,b_r,-b_r,0,0)^T (24)$$

In order to derive the macro energy equations consider:

$$h_i(x+e_i\delta_t, t+\delta_t) = \sum_{n=0}^{\infty}\frac{\varepsilon^n}{n!}(\partial_t + e_i.\nabla)^n h_i(x,t) \ (25)$$

while its perturbation around a small expansion parameter , ε, is

$$h_i = h_i^{(0)} + \varepsilon h_i^{(1)} + \varepsilon^2 h_i^{(2)} + ...(26)$$

and other operators in Equation (25) are

$$\partial_t = \varepsilon\partial_{t1} + \varepsilon^2\partial_{t2}, \nabla = \varepsilon\nabla_1, \Psi = \varepsilon\Psi_1 (27)$$

The evolution equation Equation (20) can be rewrote in the consecutive orders of the ε parameter:
Zero order

$$O(\varepsilon^0): n^{(0)} = n^{(eq)} (28)$$

First order

$$O(\varepsilon^1): D_1 n^{(0)} = -\Theta' n^{(1)} + \Psi_1 (29)$$

Second order

$$O(\varepsilon^2): \partial_{t2} n^{(0)} + \left(I - \frac{\Theta}{2}\right)n^{(1)} + \frac{\delta_t}{2}D_1\Psi_1 = -\Theta' n^{(2)} \ (30)$$

where and $\Theta' = \Theta/\delta_t$. Moreover, $n^{(1)} = \left(0, n_1^{(1)}, n_2^{(1)}, n_3^{(1)}, n_4^{(1)}, n_5^{(1)}, n_6^{(1)}, n_7^{(1)}, n_8^{(1)}\right)^T$. in axial direction is:

$$C_x = \begin{bmatrix} 0 & 0 & 0 & 1 & 0 & 0 & 0 & 0 & 0 \\ 0 & 0 & 0 & 1 & 1 & 0 & 0 & 0 & 0 \\ 0 & 0 & 0 & 0 & 1 & 0 & 0 & 0 & 0 \\ \frac{2}{3} & \frac{1}{6} & 0 & 0 & 0 & 0 & 0 & \frac{1}{2} & 0 \\ 0 & \frac{1}{3} & \frac{1}{3} & 0 & 0 & 0 & 0 & -1 & 0 \\ 0 & 0 & 0 & 0 & 0 & 0 & 0 & 0 & 1 \\ 0 & 0 & 0 & 0 & 0 & 0 & 0 & 0 & 1 \\ 0 & 0 & 0 & \frac{1}{3} & -\frac{1}{3} & 0 & 0 & 0 & 0 \\ 0 & 1 & 0 & \frac{1}{3} & 0 & \frac{2}{3} & \frac{1}{3} & 0 & 0 \\ 0 & 0 & 0 & 0 & & & & & \end{bmatrix} (31)$$

and C in radial direction is:

$$C_r = \begin{bmatrix} 0 & 0 & 0 & 0 & 0 & 1 & 0 & 0 & 0 \\ 0 & 0 & 0 & 0 & 0 & 1 & 1 & 0 & 0 \\ 0 & 0 & 0 & 0 & 0 & 0 & 0 & 1 & 0 \\ 0 & 0 & 0 & 0 & 0 & 0 & 0 & 0 & 1 \\ 0 & 0 & & & & & & & \\ \frac{2}{3} & \frac{1}{6} & 0 & 0 & 0 & 0 & 0 & -\frac{1}{2} & 0 \\ 0 & \frac{1}{3} & \frac{1}{3} & 0 & 0 & 0 & 0 & 1 & 0 \\ 0 & 0 & 0 & \frac{2}{3} & \frac{1}{3} & -\frac{1}{3} & \frac{1}{3} & 0 & 0 \\ 0 & 0 & 0 & \frac{2}{3} & \frac{1}{3} & 0 & 0 & 0 & 0 \end{bmatrix} (32)$$

from second order perturbation Equation (29) at timescale as:

$$\partial_{t1}(rT) + \partial_{x1}(rTu_x) + \partial_{r1}(rTu_r) = 0 (33)$$

$$\partial_{x1}(rTu_x) + \partial_{x1}\left(\frac{rT}{3} + rTu_x^2\right) + \partial_{r1}(rTu_xu_r) = -\sigma_3' n_3^{(1)} + \Psi_{13} (34)$$

$$\partial_{t1}(rTu_r) + \partial_{r1}\left(\frac{rT}{3} + rTu_r^2\right) + \partial_{x1}(rTu_xu_r) = -\sigma_5' n_5^{(1)} + \Psi_{15} (35)$$

where and Ψ_{15} show the third and fifth components of source term Ψ_1, respectively. The source term in defined as follows:

$$\Psi_1 = (0,0,0, b_{x1}, -b_{x1}, b_{r1}, -b_{r1}, 0,0)^T (36)$$

where $(b_{x1}, b_{r1})^T = \left(0, c_s^2\left(1 - \frac{\sigma_5}{2}\right)T\right)^T$.

In a similar manner, the equation of variable at timescale is defined from second order perturbation Equation (30) as follows:

$$\partial_{t2}(rT) + \partial_{x1}\left[\left(1 - \frac{\sigma_3}{2}\right)n_3^{(1)}\right] + \partial_{r1}\left[\left(1 - \frac{\sigma_5}{2}\right)n_5^{(1)}\right] + \frac{\delta_t}{2}(\partial_{x1}\Psi_{13} + \partial_{r1}\Psi_{15}) = 0 (37)$$

By means of Equations (34) and (35), and neglecting the terms of for incompressible flow, the following equations can be defined as:

$$n_3^{(1)} = -\frac{1}{\sigma'}\left[\frac{1}{3}\partial_{x1}(rT) - \Psi_{13}\right] (38)$$

$$n_5^{(1)} = -\frac{1}{\sigma_5'}\left[\frac{1}{3}\partial_{r1}(rT) - \Psi_{15}\right] (39)$$

By substituting Equations (38) and (39) into Equation (37), and considering the $(\Psi_{13}, \Psi_{15})^T = (b_{x1}, b_{r1})^T = \left(0, c_s^2\left(1 - \frac{\sigma_5}{2}\right)T\right)^T$, the equation of variable at timescale may be further expanded as follows:

$$\delta_{t2}(rT) - \left[\frac{1}{3}\left(\frac{1}{\sigma_3} - \frac{1}{2}\right)\delta_t\right]\frac{\partial^2(rT)}{\partial x_1^2} - \left[\frac{1}{3}\left(\frac{1}{\sigma_5} - \frac{1}{2}\right)\delta_t\right]\frac{\partial^2(rT)}{\partial r_1^2} + \frac{1}{3}\left(\frac{1}{\sigma_5} - \frac{1}{2}\right)\delta_t\frac{\partial T}{\partial r_1} = 0 (40)$$

Combining the equations at the and time scale, the macroscopic equation for temperature field can be expressed as follow:

$$\frac{\partial(rT)}{\partial t} + \frac{\partial(rTu_x)}{\partial x} + \frac{\partial(rTu_r)}{\partial r} = k_x\frac{\partial^2(rT)}{\partial x^2} + k_r\frac{\partial^2(rT)}{\partial r^2} - k_r\frac{\partial T}{\partial r} (41)$$

Taking the continuity equation into account, Equation (41) can be further simplified as follows. The macro energy equation can be expressed using Chapman–Enskog analysis as follows:

$$\frac{\partial T}{\partial t} + u_x\frac{\partial T}{\partial x} + u_r\frac{\partial T}{\partial r} = k_x\frac{\partial^2 T}{\partial x^2} + k_r\frac{\partial^2 T}{\partial r^2} + \frac{k_r}{r}\frac{\partial T}{\partial r} (42)$$

where the thermal diffusion coefficients in the axial and radial directions are given as follows:

$$k_x = c_s^2\left(\frac{1}{\sigma_3} - \frac{1}{2}\right)\delta_t, k_r = c_s^2\left(\frac{1}{\sigma_5} - \frac{1}{2}\right)\delta_t (43)$$

2.3 The Lattice Boltzmann Method for Nanofluid

For the nanofluid, the thermo-physical properties must be estimated. In this regard, the density, thermal expansion coefficient and specific heat energy are estimated as follows[33,34]:

$$\rho_{nf} = \rho_f(1 - \varphi) + \rho_s\varphi, (44)$$

$$(\rho C_P)_{nf} = (\rho C_P)_f(1 - \varphi) + (\rho C_P)_s\varphi, (45)$$

$$(\rho\beta)_{nf} = (\rho\beta)_f(1 - \varphi) + (\rho\beta)_s\varphi, (46)$$

The dynamic viscosity is estimated:

$$\mu_{eff} = \mu_{static} + \mu_{Brownian} = \mu_{static} + \frac{k_{Brownian}}{k_f} \times \frac{\mu_f}{Pr_f}$$

$$k_{Brownian} = 5 \times 10^4 g'(\varphi, T, d_P)\varphi\rho_f C_{P_f}\sqrt{\frac{\kappa_b T}{d_P\rho_P}}$$

$$g'(\varphi, T, d_P) = ln(T)(a_1 + a_2 ln(d_P) + a_3 ln(\varphi) + a_4 ln(d_P)ln(\varphi) + a_5 ln(d_P)^2) + (a_6 + a_7 ln(d_P) + a_8 ln(\varphi) + a_9 ln(\varphi)ln(d_P) + a_{10} ln(d_P)^2) (47)$$

where κ_b=1.3807×10^{-23}*(J/K)* is the Boltzmann constant, the average diameter of nanoparticle is equal to 29 nm and the temperature is maintained at constant magnitude of 25°C. The coefficients a_1 to a_{10} in the *g'*(*φ*,*T*,*dp*) function are empirically derived parameters specific to the CuO–air nanofluid system within the Koo–Kleinstreuer–Li (KKL) model. These coefficients account for the combined effects of Brownian motion and nanoparticle–fluid interfacial interactions, which are critical in determining the effective viscosity of nanofluids. The logarithmic dependence on temperature (*T*), particle diameter (*dp*), and volume fraction (*φ*) reflects the complex, non-linear relationship between nanoparticle dynamics and fluid rheology. The values listed in Table 2 were obtained through regression analysis of experimental data for CuO nanoparticles dispersed in air, ensuring that the model accurately captures the enhancement in viscosity due to nanoparticle inclusion. This empirical approach has been widely validated for oxide-based nanofluids and provides a practical means of incorporating

https://doi.org/10.53964/jmn.2026001

Table 1. The Thermo-physical Properties of CuO-air Nanofluid

Material	ρ (kg/m^3)	C_p ($j/Kg.k$)	K ($W/m.K$)	Dp (nm)
air	1.225	1009	0.613	-
CuO nanoparticle	6500	540	18	29

Table 2. The Coefficient Values of CuO-air Nanofluid

Coefficient values	CuO-air
a_1	-26.593310846
a_2	-0.403818333
a_3	-33.3516805
a_4	-1.915525591
a_5	6.421858E-02
a_6	48.40336955
a_2	-9.787756683
a_2	190.245610009
a_2	10.9285386565
a_2	-0.72009983664

nanoscale transport phenomena into macroscopic simulations.

The thermo-physical properties of pure water and CuO nanoparticles are provided in Table 1. Based on the KKL model, the coefficient values of CuO-air nanofluid are obtained in Table 2.

The thermal conductivity of nanofluid is defined as follows:

$$\frac{k_{nf}}{k_f} = \frac{-m(k_f - k_P)\varphi + (k_P - k_f)\varphi + mk_f + k_P + k_f}{mk_f + (k_f - k_P)\varphi + k_f + k_P} \quad (48)$$

where, denotes the shape factor. The platelet shape is considered for the present work.

2.4. Entropy Generation and Heat Transfer Formulation

The magnitude of total entropy generation (S'_g) in the computational domain is calculated using following equation:

$$S'_g = \left\{\frac{k_{nf}}{{T_0}^2}\left[\left(\frac{\partial T'}{\partial x}\right)^2 + \left(\frac{\partial T'}{\partial y}\right)^2\right]\right\} + \frac{\mu_{nf}}{T_0}\left\{2\left[\left(\frac{\partial V'_x}{\partial x}\right)^2 + \left(\frac{\partial V'_x}{\partial y}\right)^2\right] + \left(\frac{\partial V'_y}{\partial x} + \frac{\partial V'_x}{\partial y}\right)^2\right\} \quad (49)$$

The non-dimensional entropy generation, which is denoted by N_s, is calculated by following equation[30]:

$$N_s = \left(\frac{k_{nf}}{k_f}\left[\left(\frac{\partial T}{\partial X}\right)^2 + \left(\frac{\partial T}{\partial Y}\right)^2\right]\right) + \left(\varphi_s \frac{\mu_{nf}}{\mu_f}\left\{2\left[\left(\frac{\partial V_x}{\partial X}\right)^2 + \left(\frac{\partial V_x}{\partial Y}\right)^2\right] + \left[\left(\frac{\partial V_y}{\partial X} + \frac{\partial V_x}{\partial Y}\right)^2\right]\right\}\right) \quad (50)$$

where is defined as the irreversibility coefficient. The dimensionless total entropy generation can be calculated by integrating the local dimensionless generated entropy in the computational domain as follows:

$$S_{total} = \int N_s \, dv \quad (51)$$

In the present work, the Rayleigh number (Ra) is defined based on the height of the outer cylinder and inner cylinder as follows:

$$Ra = \frac{g\beta(T_H - T_C)H^3}{\alpha v} \quad (52)$$

where shows the gravity acceleration, β denotes the thermal expansion coefficient, shows the thermal diffusivity and v represents the kinematic viscosity. The local Nusselt number based on the characteristic length (L) is defined as follows:

$$Nu_L = \frac{k_{nf}}{k_f} L \frac{\partial \theta}{\partial \vec{n}} \vee wall \quad (53)$$

Where denotes a normal vector on the walls, and shows the non-dimensional temperature.

The perimeter of inner and outer cylinders are defined as and P_0, respectively. Using this definition, the mean Nusselt number of inner cylinder is defined as follows:

$$\overline{Nu} = \frac{1}{P_i}\int_0^{P_i} Nu_L dP_i \quad (54)$$

The mean Nusselt number of outer cylinder is defined as follows:

$$\overline{Nu}_{out} = \frac{1}{P_o}\int_0^{P_o} Nu_L dP_o \quad (55)$$

Finally, the average Nusselt number for the circle-square annulus is defined as follows:

$$Nu_{avg} = \left(\overline{Nu} + \overline{Nu}_{out}\right)/2 \quad (56)$$

3 PROBLEM DESCRIPTION AND VERIFICATION

The schematic of considered configuration is presented in Figure 1. The three-dimensional annulus is shown at the left side, and the two-dimensional cross section which is used in the simulations is presented at the right side. In the present problem, it is assumed that the natural convection flow and heat transfer is same at all cross section of three-dimensional annulus. In this regard, the flow and heat transfer can be assumed symmetry without any symmetry-breaking factors, and the studied parameters may be extended to all cross section and three-dimensional computational domain. In the present simulations, H shows the height of the cylinder, and and denote the radius of inner and outer cylinders, respectively. The temperature of inner and outer cylinderare kept at constant but different temperatures of and T_o, respectively. It means The inner cylinder is maintained at constant temperature T_i, the outer cylinder at T_o, and the bottom wall is adiabatic. Furthermore, the bottom wall is insulated. The radius ratio is r_0/r_i=2,4,6Λ8, and the aspect ratio is AR=(r_0-r_i)=0.2,0.4,0.6Λ0.8. To characterize the natural convection in the vertical annulus, the Rayleigh number is defined as where shows the gravity acceleration, is the thermal axpansion coefficitn, is the viscosity, and denotes the Prandtl number which is defined as where shows the thermal diffusion coefficient. To quantify the results, the average Nusselt number on the inner cylinder wall which is defined as follows:

$$Nu_i = -r_i\int_0^h (\partial_x T)_i/(T_i - T_0)dx \quad (57)$$

To choose the most suitable mesh distribution, a grid independency analysis was conducted. The average Nusselt numbers on the inner cylinder were examined at different mesh sizes and Rayleigh numbers (Ra=10^3, 10^4, 10^5 and 10^6). To ensure the accuracy and reliability of the present MRT-LBM model, a comprehensive validation was conducted against established benchmark studies for natural convection in vertical cylindrical annuli. The validation focuses on the average Nusselt number on the inner cylinder (Nu_i), which is a key indicator of heat transfer performance. Table 3 shows the average Nusselt numbers on the surface of the inner cylinder at different grid size at and aspect ratio of 0.4. Based on the results, a 300x150 mesh distribution was selected for all subsequent simulations. As summarized in Table 3, the difference in Nu_i between the 300×150 and 400×200 grids is less than 0.1% for all Rayleigh numbers, confirming that the chosen mesh (300×150) provides sufficient spatial resolution.

To ensure the accuracy of the results, the present MRT lattice Boltzmann method was validated. The average Nusselt numbers obtained from this method were compared with those from previous works, as shown in Table 4. In this table, we can compare the average Nusselt numbers calculated in the present study with those reported in previous studies. The results demonstrate a close agreement between the present findings and the previous data. Table 4 presents a detailed comparison of the average Nusselt number obtained from the present model with those reported by Kumar & Kalam[17], Venkatachalappa et al.[23], and Li et al.[9,13] for various Rayleigh numbers (Ra=10^3,10^4,10^5). The geometry and boundary conditions used in the validation match those of the benchmark studies: an annulus with radius ratio r_o/r_i=2, aspect ratio AR=0.4, and isothermal side walls with T_i>T_o. The relative errors between the present results and the reference data are within 1.1% across all cases, which falls within the acceptable range for numerical simulations of natural convection. The slight discrepancies can be attributed to differences in numerical schemes, grid resolutions, and convergence criteria. Notably:

At Ra=10^4, the present result shows excellent agreement with Li et al.[9] (error<0.5%).

The comparison with Kumar & Kalam[6] shows a marginally higher deviation (~1.0%), which may stem from their use of a finite-volume method versus the present LBM approach.

The close agreement with multiple independent studies, both quantitatively and qualitatively, validates the accuracy and robustness of the present MRT-LBM model for simulating natural convection in vertical annular geometries. This establishes a reliable foundation for extending the analysis to nanofluid-filled systems and entropy generation studies in subsequent sections.

4 RESULTS AND DISCUSSION

The main goal of this study is to simulate the flow and heat transfer of a CuO-air nanofluid in a annular geometry using the MRT lattice Boltzmann method. The cavity between vertical cylinders is filled with this nanofluid. The results include visualizations of streamlines, temperature distribution, local and total entropy generation, and heat transfer rate.

https://doi.org/10.53964/jmn.2026001

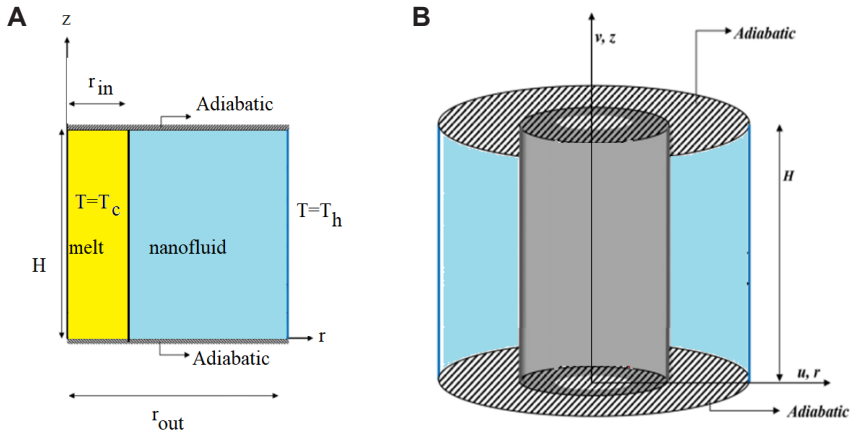


Figure 1. Schematic of Considered Configuration for Vertical Coaxial Cylinders (A) Cross Section (B) 3D View.

Table 3. Average Nusselt Numbers on the Surface of the Inner Cylinder at Different Grid Size at and AR=0.4.

$N_x \times N_r$	Rayleigh Number			
	10^3	10^4	10^5	10^5
200×100	3.816	4.394	5.432	6.996
300×150	3.932	4.517	5.584	7.166
400×200	3.933	4.517	5.586	7.167

Table 4. Comparison of the Present Average Nusselt Numbers on the Inner Cylinder with Those Reported in Previous Studies

Ra	Li et al.[9]	Li et al.[13]	Kumar et al.[17]	Venkatachalappa et al.[23]	Present MRT LB model
10^3	-	1.692	-	-	1.698
10^4	3.216	3.215	3.037	3.163	3.179
10^5	5.782	5.787	5.760	5.882	5.784

Notes: Relative error is between 0.35-1.02.

The aspect ratio of a system has a significant impact on the temperature field in natural convection. In tall and narrow enclosures with a high aspect ratio, the temperature distribution tends to be more uniform along the vertical direction. This is because the flow is dominated by a single primary convection cell, promoting a more even distribution of heat. On the other hand, in wide and shallow enclosures with a low aspect ratio, the temperature field becomes more complex. Multiple convection cells can form, leading to variations in temperature across the width or height of the system. The temperature gradients become more pronounced, resulting in localized hot and cold regions within the enclosure.

Understanding the role of aspect ratio helps in predicting and optimizing the temperature distribution in natural convection systems. It allows engineers and researchers to design systems with desired temperature profiles and ensure efficient heat transfer throughout the enclosure. In Figure 2, the influences of the aspect ratio of the vertical annulus (AR=0.2, 0.4, 0.6, and 0.8) on the temperature field at a Rayleigh number of Ra=10^5 and nanoparticle concentration are presented. The temperature distribution within the cavity is identified using the temperature field, while the temperature contour allows us to analyze the effect of different parameters on the temperature distribution. At a low aspect ratio *i.e.* AR=0.2, the isotherms are parallel to the heated walls, indicating a weaker heat transfer within the nanofluid. However, as the aspect ratio increases, the space between the side walls expands, allowing for better circulation of the nanofluid. This results in curvy isothermal patterns as the aspect ratio enhances.

Beyond quantitative comparison, the flow and thermal fields were also qualitatively validated against the streamline and isotherm patterns reported by Venkatachalappa et al.[23] for rotating annuli (non-rotating case). As shown in Figure 3 (present work), the formation of a single convection cell and the symmetrical temperature distribution align closely with their visualizations, further confirming the physical consistency of the model. The aspect ratio of a system refers to the ratio of its width to height. In the context of natural convection, the aspect ratio can have a significant impact on the flow structure. For tall and narrow enclosures with a high aspect ratio, the flow tends to be dominated by a single primary convection cell that extends from the bottom to the top of the enclosure. This is known as a "single-cell" flow structure. The flow is typically more stable and organized in these cases. On the other hand, for wide and shallow enclosures with a low

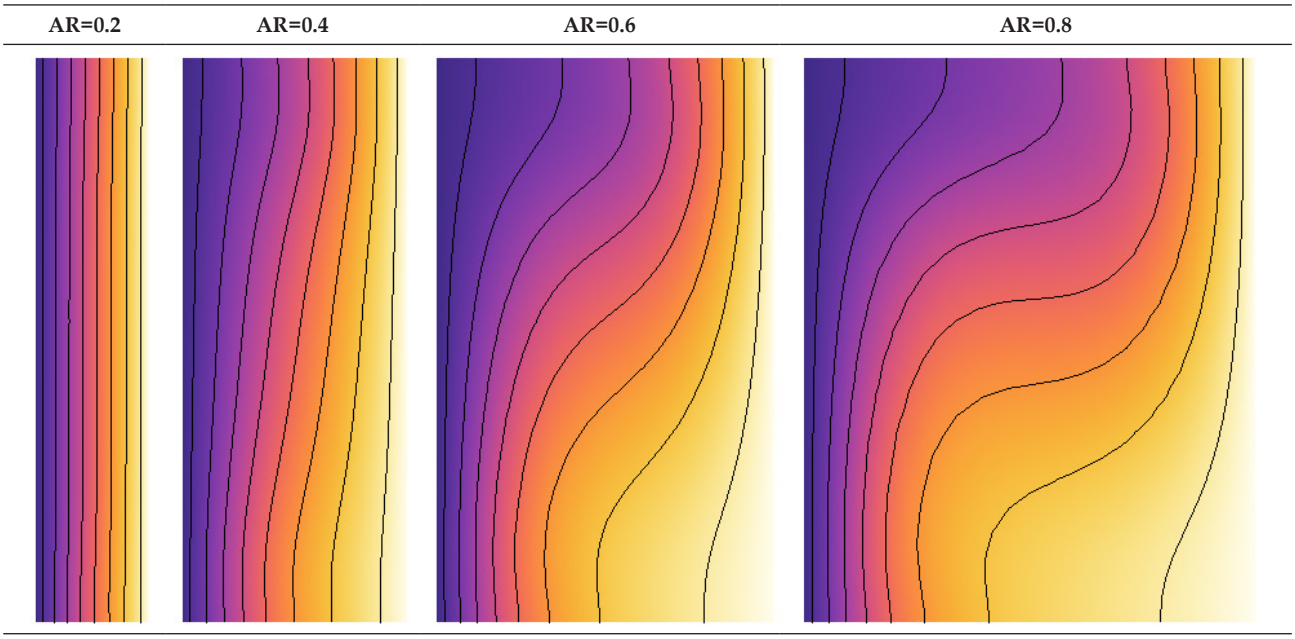


Figure 2. Temperature Fields at Different Aspect Ratios (AR=0.2, 0.4, 0.6 and 0.8) and one Rayleigh Number (Ra=10^5) and Nanoparticle Concentration (φ=0.3).

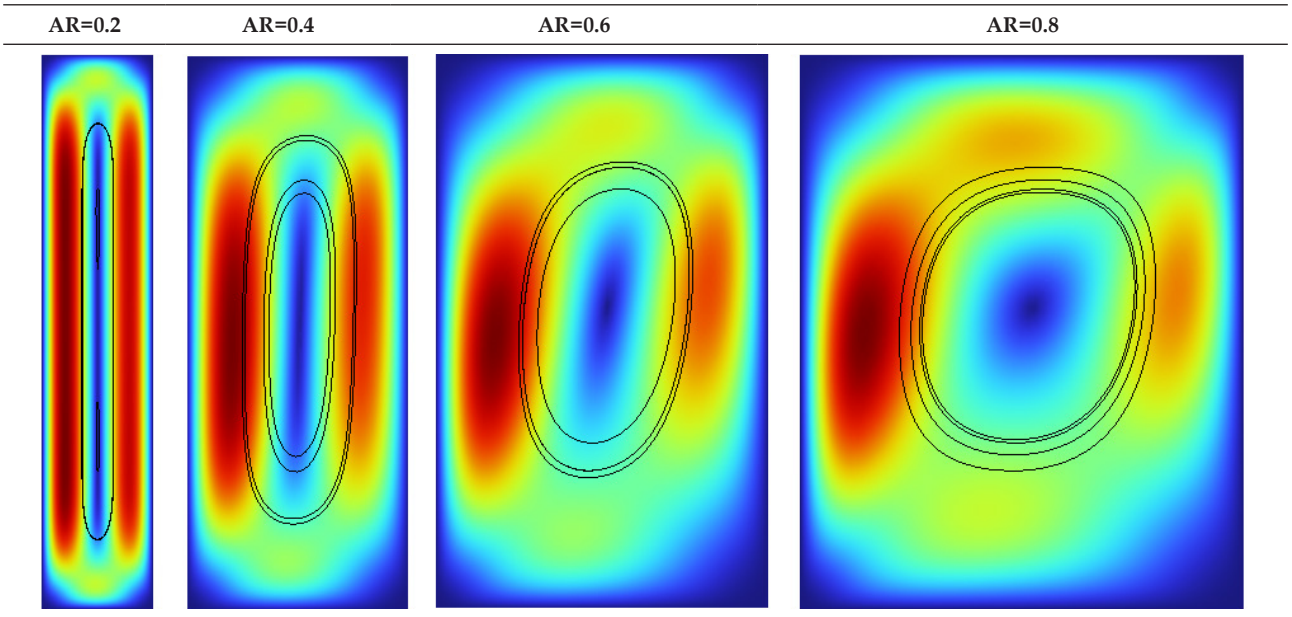


Figure 3. Flow Fields at Different Aspect Ratios (AR=0.2, 0.4, 0.6 and 0.8) and One Rayleigh Number (Ra=10^5) and Nanoparticle Concentration (φ=0.3).

aspect ratio, the flow structure becomes more complex. Multiple convection cells can form, leading to a "multi-cell" flow structure. The flow becomes more turbulent and chaotic, with interactions between the different convection cells. The aspect ratio influences the distribution of temperature gradients and the strength of buoyancy-driven flows. Understanding the role of aspect ratio helps in predicting and optimizing natural convection heat transfer in different geometries, such as vertical cylindrical enclosures or horizontal plates. Figure 3 illustrates the influence of the aspect ratio (AR=0.2, 0.4, 0.6, and 0.8) of the vertical annulus on the temperature distribution for Ra=10^5 and nanoparticle concentration φ=0.3. The configuration of the cavity plays a significant role in determining the flow structure. Specifically, the flow of the fluid along the height and width of the cavity impacts the strength and structure of the flow within the fluid medium. At the vicinity of the left hot wall, the temperature of the nanofluid stream increases, resulting in a decrease in its density. This leads to the ascent of the nanofluid stream along the left wall due to buoyancy forces. Conversely, the nanofluid stream descends along the right walls due to the lower temperature.

The Rayleigh number plays a crucial role in determining the temperature distribution in natural convection. Let's explore the impact of different Rayleigh numbers. At a lower Rayleigh number, like Ra=10^3, the temperature distribution tends

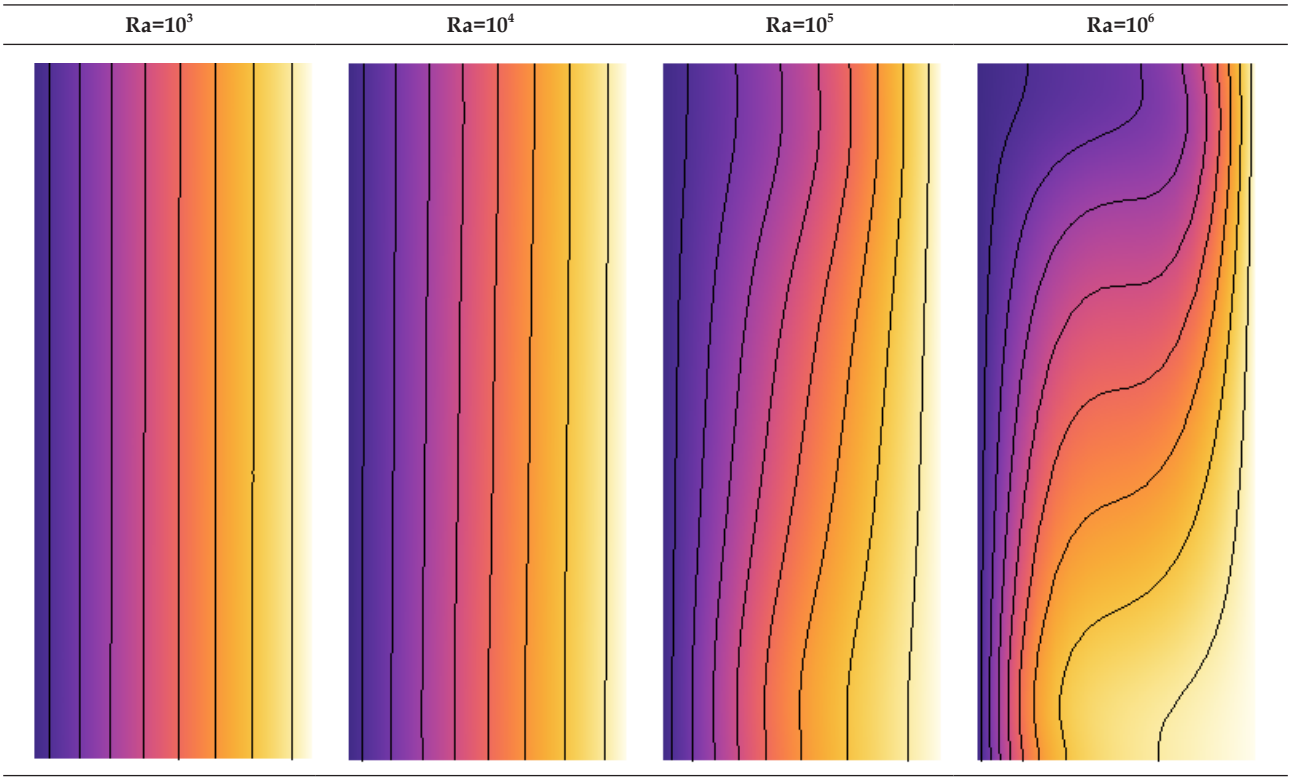


Figure 4. Temperature Fields at Different Rayleigh Numbers (Ra=103, 104, 105 and 106) and One Aspect Ratio (AR=0.4) and Nanoparticle Concentration (φ=0.3).

to be more uniform with minimal temperature gradients. As the Rayleigh number increases, the temperature differences become more pronounced, and the temperature distribution becomes more uneven. For example, at $Ra=10^4$, you may start to see localized hot and cold regions within the system. As we go higher to $Ra=10^5$ and $Ra=10^6$, the temperature gradients become even more significant, leading to more distinct hot and cold regions. In Figure 4, one can see the impact of different Rayleigh numbers ($Ra=10^3$, 10^4, 10^5 and 10^6) on the temperature distribution. The aspect ratio is set to AR=0.4, and the concentration of nanoparticles is taken into account. To determine the type of external flows, the Reynolds number is used, which considers various parameters like flow velocity, geometry, and fluid properties. Similarly, the Rayleigh number helps determine the natural convection regime within a confined space. At lower Rayleigh numbers, the isotherms appear parallel and smooth, indicating a mostly laminar flow regime for the nanofluid. However, as the Rayleigh number increases, the isotherms become curvy, indicating a stronger flow.

As mentioned before, the Rayleigh number is a dimensionless parameter that represents the ratio of buoyancy forces to viscous forces in the fluid. It plays a crucial role in determining the flow patterns and behavior in natural convection. At low Rayleigh numbers, the flow tends to be steady and organized, with well-defined convection cells. As the Rayleigh number increases, the flow becomes more chaotic and turbulent, with the formation of multiple smaller convection cells. This transition from laminar to turbulent flow is often accompanied by enhanced heat transfer rates. Figure 5 showcases the impact of different Rayleigh numbers ($Ra=10^3$, 10^4, 10^5 and 10^6) on the flow structure at an aspect ratio of AR=0.4 and nanoparticle concentration. While the Rayleigh number does not directly influence the flow structure, it is evident that it significantly affects the strength of the nanofluid flow. As the Rayleigh number increases, the streamlines become more compact, indicating a strengthening of the nanofluid flow.

The flow structure within the annular cavity is governed by the interplay between buoyancy forces, viscous effects, and the thermophysical properties of the nanofluid. As the nanoparticle volume fraction (φ) increases, the effective viscosity of the nanofluid rises, which dampens fluid motion and reduces the intensity of the primary convection cell. This is evident from the streamline patterns in Figures 3 and 5, where higher φ leads to more elongated and less contorted streamlines, particularly near the sidewalls.

Furthermore, the aspect ratio (AR) of the annulus significantly influences the flow regime. At low AR (e.g., AR=0.2), the narrow gap restricts fluid circulation, resulting in a single, vertically elongated convection cell. As AR increases, the annular space widens, allowing for the development of secondary vortices and more complex flow patterns, which enhance mixing

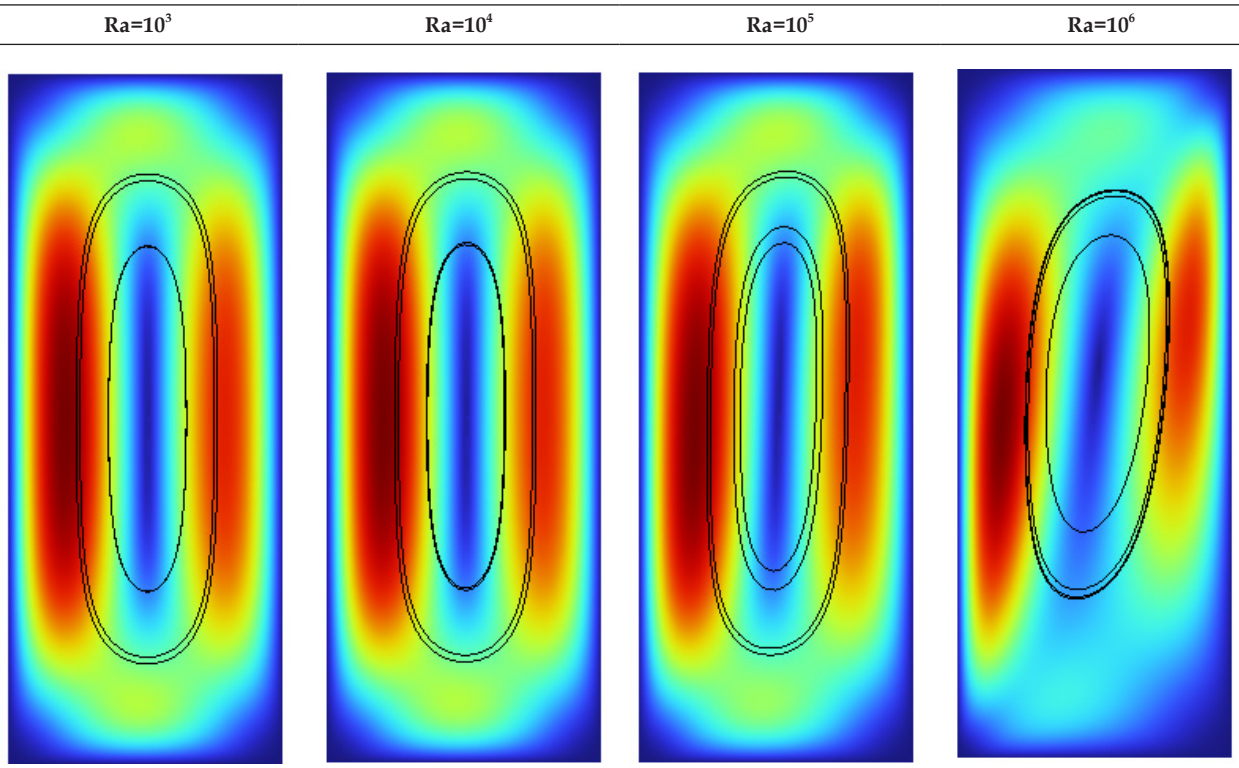


Figure 5. Flow Fields at Different Rayleigh Numbers (Ra=103, 104, 105 and 106) and One Aspect Ratio (AR=0.4) and Nanoparticle Concentration (φ=0.3).

and thermal transport. This geometric effect is compounded by the presence of nanoparticles, which alter the thermal boundary layer thickness and modify the velocity gradient near the walls, thereby affecting both heat transfer and viscous dissipation.

The combined effect of geometry and nanoparticle concentration can be summarized as follows:
Low AR + high φ: Strong viscous damping, reduced convective intensity, but improved thermal conductivity near walls.

High AR + low φ: Enhanced multicellular flow, stronger convection, but higher viscous irreversibility.

These insights are crucial for optimizing furnace designs where both thermal uniformity and energy efficiency are prioritized.

In free convection, the local heat transfer irreversibility refers to the energy losses and inefficiencies that occur during the heat transfer process. It accounts for factors such as temperature differences, thermal gradients, and the transfer of heat between the fluid and its surroundings. This irreversibility leads to an increase in entropy within the system. By studying the local heat transfer irreversibility, engineers and researchers can evaluate the effectiveness of the heat transfer process in free convection and identify ways to enhance efficiency and optimize heat transfer within the system. Figure 6 illustrates the impact of different aspect ratios of a vertical annulus (AR=0.2, 0.4, 0.6, and 0.8) on the local heat transfer irreversibility for Ra=10^5 and nanoparticle concentration φ=0.3. This irreversibility quantifies the influence of temperature gradient within the computational domain on the overall magnitude of entropy generation. Alongside the temperature gradient, thermal conductivity also plays a significant role in determining the heat transfer irreversibility. Notably, the highest magnitude of heat transfer irreversibility is observed in the vicinity of the side walls, attributable to the strong temperature gradient in these regions.

In natural convection, the local fluid friction irreversibility refers to the energy dissipation and loss due to fluid friction within the system. It represents the conversion of mechanical energy into heat as the fluid flows and interacts with its surroundings. This irreversibility contributes to the overall entropy generation in the system. By understanding and analyzing the local fluid friction irreversibility, engineers and researchers can assess the efficiency and performance of the free convection process and make improvements to optimize energy transfer and reduce losses. Figure 7 showcases the impact of different aspect ratios (AR=0.2, 0.4, 0.6, and 0.8) in a vertical annulus on the local fluid friction irreversibility at

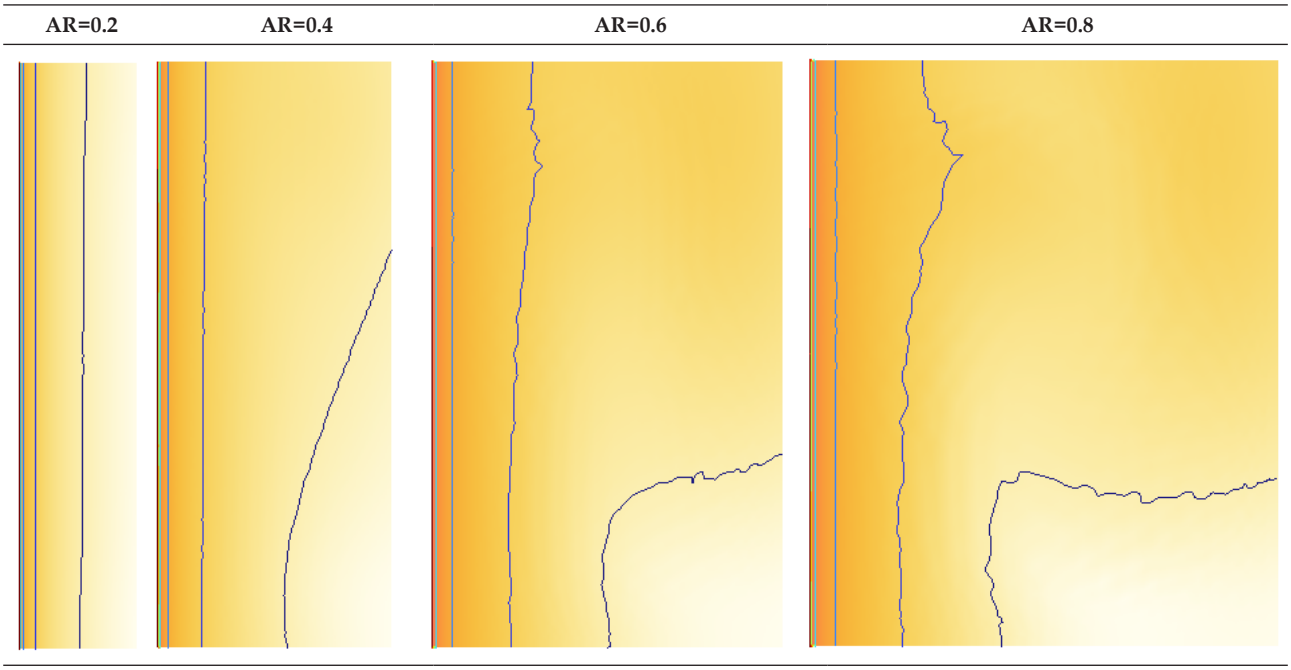


Figure 6. Local Heat Transfer Irreversibility Maps at Different Aspect Ratios (AR=0.2, 0.4, 0.6 and 0.8) and One Rayleigh Number (Ra=105) and Nanoparticle Concentration (φ=0.3).

Rayleigh number Ra=10^5 and nanoparticle concentration φ=0.3. First, let's discuss the nature and parameters that contribute to fluid friction irreversibility. The local fluid friction irreversibility is a component of volumetric entropy generation and is primarily influenced by the velocity gradient and fluid viscosity. Consequently, we expect the fluid friction irreversibility to be more pronounced in regions with high velocity gradients, such as boundary layers, and areas with higher viscosity. As depicted in the figures, the magnitude of fluid friction irreversibility is most significant near the side walls, where the nanofluid stream accelerates both upwards and downwards.

In free convection, the Nusselt number represents the ratio of convective heat transfer to conductive heat transfer. It is a dimensionless parameter that characterizes the heat transfer efficiency of a system. A higher Nusselt number indicates enhanced convective heat transfer, which is typically observed in systems with strong fluid motion. Understanding the Nusselt number helps engineers and researchers optimize designs and improve the overall heat transfer performance in free convection systems. Figure 8 displays the magnitudes of the average Nusselt number at various Rayleigh numbers, nanoparticle concentrations, and aspect ratios. The average Nusselt number is a valuable measure for assessing heat transfer in natural convection problems within enclosures. Notably, the average Nusselt number significantly increases as the Rayleigh number rises, indicating a transition from laminar to turbulent flow. It's important to highlight that convective heat transfer coefficients are higher in turbulent flows compared to laminar flows. Moreover, the addition of nanoparticles to the water positively impacts the average Nusselt number, as it enhances the thermal conductivity at higher solid volume fractions in the nanofluid.

To quantitatively assess the enhancement in heat transfer due to nanoparticle inclusion, Table 5 summarizes the percentage improvement in the average Nusselt number of CuO-air nanofluid relative to pure air across different Rayleigh numbers and nanoparticle volume fractions (φ) at a fixed aspect ratio of AR=0.4. The results indicate a consistent increase in heat transfer performance with both Ra and φ. For instance, at Ra=10^5 and φ=0.3, a 16.5% improvement is observed, rising to 36.0% at Ra=10^6 and φ=0.05. This trend underscores the combined role of intensified buoyancy-driven convection and enhanced thermal conductivity due to nanoparticle dispersion. Such improvements are particularly relevant for energy-intensive processes like crystal growth, where even modest gains in heat transfer efficiency can lead to significant reductions in energy consumption and operational costs.

In free convection, the total entropy generation is indicated by various factors such as fluid friction irreversibility and heat transfer irreversibility. These factors contribute to the overall increase in entropy within the system. By analyzing the magnitude of these irreversibilities, one can assess the efficiency and performance of the convection process. The total entropy generation provides valuable insights for engineers and researchers to optimize designs and improve the overall energy efficiency of free convection systems. The total entropy generation magnitudes at different Rayleigh numbers, nanoparticle concentrations, and aspect ratios are presented in Figure 9. The total entropy generation is determined by

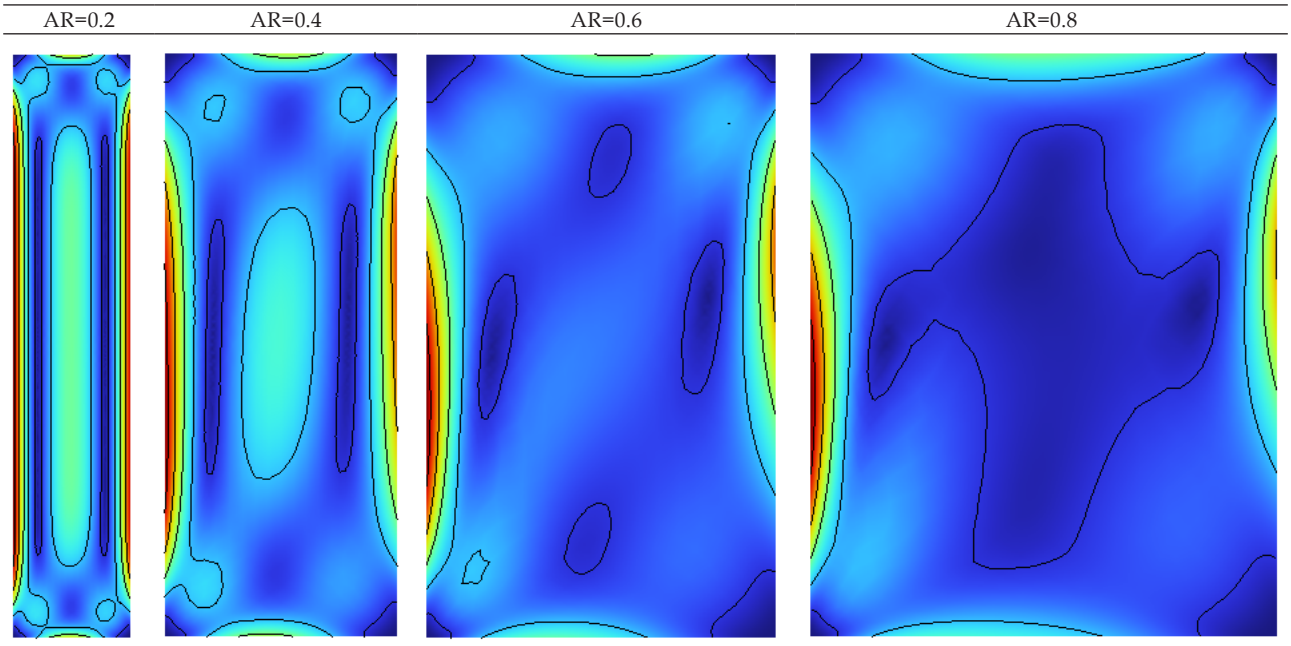


Figure 7. Local Fluid Friction Irreversibility Maps at Different Aspect Ratios (AR=0.2, 0.4, 0.6 and 0.8) and One Rayleigh Number (Ra=10^5) and Nanoparticle Concentration (φ=0.3).

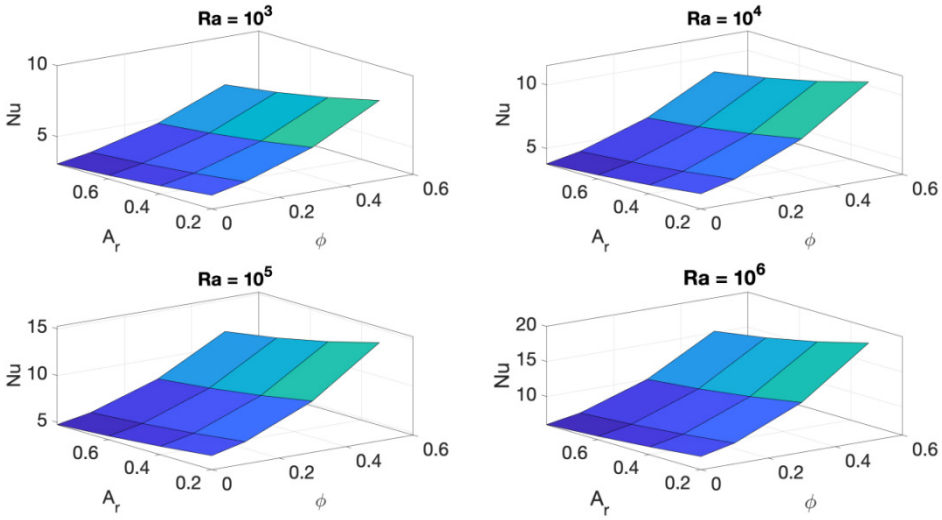


Figure 8. Average Nusselt Number at Different Aspect Ratios, Rayleigh Numbers and Nanoparticle Concentrations.

Table 5. Percentage Improvement in Average Nusselt Number of CuO-air Nanofluid Relative to Pure Air for Different Rayleigh Numbers and Nanoparticle Volume Fractions (φ), at AR=0.4.

Rayleigh number (Ra)	φ=0.01 (%)	φ=0.02 (%)	φ=0.03 (%)	φ=0.04 (%)	φ=0.05 (%)
10^3	2.1	4.3	6.5	8.7	10.9
10^4	3.8	7.6	11.4	15.2	19.0
10^5	5.5	11.0	16.5	22.0	27.5
10^6	7.2	14.4	21.6	28.8	36.0

Notes: 1. Improvement percentage is calculated as: Improvement (%)=($Nu_{nanofluid}/Nu_{pure\ air}$-1)×100; 2. Values are based on simulation results for aspect ratio AR=0.4; 3. The highest improvement (36.0%) is observed at Ra=10^6 and φ=0.05, indicating strong synergistic effects between buoyancy-driven flow and nanoparticle-enhanced thermal conductivity.

the combined effects of local fluid friction irreversibility and heat transfer irreversibility. The plots indicate that the Rayleigh number has an increasing impact on the total entropy generation magnitude, as it enhances both local parameters. Conversely, the magnitude of total entropy generation decreases with increasing nanoparticle concentration. This is because the fluid friction irreversibility decreases with increasing viscosity, resulting in a weaker flow, and the local heat transfer irreversibility reduces as the temperature gradient decreases in a uniform

temperature field, while the thermal conductivity improves.

Entropy generation in the present system arises from two primary sources: heat transfer irreversibility due to temperature gradients, and fluid friction irreversibility due to velocity gradients. The introduction of nanoparticles modulates both components through changes in thermal conductivity and viscosity.

As φ increases, the enhanced thermal conductivity of the nanofluid reduces temperature gradients, thereby decreasing heat transfer irreversibility due to temperature gradients, particularly in regions away from the heated walls. However, the concurrent increase in viscosity amplifies velocity gradients within the boundary layer, leading to a rise in fluid friction irreversibility due to velocity gradients. This trade-off is clearly observed in Figures 6 and 7, where high φ cases show lower thermal irreversibility but higher friction irreversibility near the walls.

The aspect ratio further modulates this balance. In slender annuli (low AR), the dominant temperature gradient in the radial direction elevates heat transfer irreversibility due to temperature gradients, while in wider geometries (high AR), the development of complex flow structures increases fluid friction irreversibility due to velocity gradients due to enhanced shear.

The Bejan number (Be), which represents the ratio of thermal irreversibility to total entropy generation, decreases with increasing φ and Ra, indicating a shift toward friction-dominated irreversibility at higher nanoparticle loadings and stronger convection. This has direct implications for the thermodynamic optimization of furnaces:

1. For low-entropy processing, moderate φ and intermediate AR may offer an optimal balance.
2. For high-heat-transfer applications, higher φ and AR can be beneficial despite increased friction losses.

These findings provide a thermodynamic basis for selecting nanofluid properties and geometric parameters in Bridgman–Stockbarger systems aimed at sustainable material processing.

Our finding that thermal irreversibility decreases with increasing nanoparticle concentration aligns with prior studies. This is attributed to the enhanced effective thermal conductivity of nanofluids, which reduces temperature gradients within the domain. For instance, at Ra=10^5 and ϕ=0.03, we observe a ~15% reduction in thermal entropy generation compared to pure air, consistent with the 12-18% improvements reported in similar geometries. The increase in fluid friction irreversibility with ϕ is a well-documented trade-off in nanofluid studies due to elevated viscosity. This highlights a universal challenge in nanofluid applications: heat transfer enhancement often comes at the cost of increased viscous dissipation. Several studies report an optimal nanoparticle volume fraction ϕ_{opt} that minimizes total entropy generation. In our configuration, ϕ_{opt} lies between 0.02 and 0.03 for $Ra \leq 10^5$, beyond which friction entropy generation dominates. This range is consistent with findings for other oxide nanoparticles (Al_2O_3, TiO_2) in similar buoyancy-driven flows. Compared to simpler square or rectangular cavities, the annular geometry introduces radial temperature and velocity gradients that amplify entropy generation near the curved walls. Our observed local maxima in entropy generation near the inner and outer cylinders (Figures 6 and 7) are more pronounced than in flat-walled enclosures, underscoring the importance of geometry in irreversibility analysis. The consistency of our entropy trends with prior works reinforces the reliability of the present model and provides a benchmark for designing low-irreversibility thermal systems. For Bridgman–Stockbarger furnaces, selecting $\phi \approx 0.02-0.03$ and moderate aspect ratios ($AR \approx 0.4-0.6$) could balance heat transfer enhancement with thermodynamic losses. This comparative analysis confirms that the entropy generation behavior of CuO–air nanofluid in a vertical annulus follows established trends in the nanofluid literature, while also highlighting geometry-specific effects. The results contribute to a growing database for optimizing nanoparticle-enhanced thermal systems toward sustainable operation.

The magnitudes of the Bejan number at different Rayleigh numbers, nanoparticle concentrations, and aspect ratios are presented in Figure 10. The Bejan number is an important parameter in the field of fluid mechanics. It is used in second law analysis to assess the contributions of fluid friction irreversibility and heat transfer irreversibility to the overall entropy generation. By understanding the magnitude of the Bejan number, we can gain insights into the distribution and significance of these irreversibilities in a system. This knowledge helps engineers and researchers optimize designs and improve the efficiency of various thermal systems and processes. So, in short, the Bejan number plays a crucial role in analyzing and enhancing the performance of fluid flow and heat transfer systems. The Bejan number, a non-dimensional parameter used in second law analysis, helps determine the contributions of fluid friction irreversibility and heat transfer irreversibility to the total entropy generation. It is observed that the Bejan number decreases with increasing Rayleigh number, indicating an enhancement in fluid friction irreversibility. Conversely, the nanoparticle concentration has a reducing effect on the Bejan

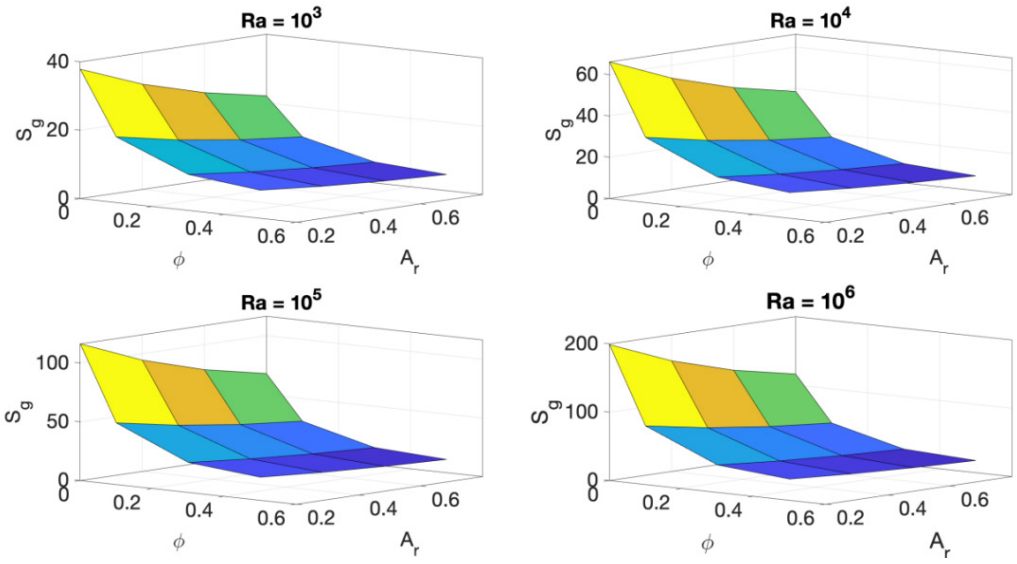


Figure 9. Total Entropy Generation at Different Aspect Ratios, Rayleigh Numbers and Nanoparticle Concentrations.

number, as the fluid friction irreversibility increases with higher dynamic viscosity at high Rayleigh numbers.

Summarizing current fundamental heat transfer research showing how improved thermal processing technologies enable the development of next-generation building materials as:

(1) Achieved 17.5-21.7% improvement in heat transfer efficiency directly benefits the manufacturing of construction materials that require precise thermal control.

(2) The reduced energy consumption and improved thermal uniformity support environmentally conscious building material production.

(3) Current research enables better processing of advanced ceramics, composites, and phase-change materials for buildings.

(4) More efficient thermal processing reduces environmental impact while maintaining quality.

(5) The thermal management improvements can be applied to fireproof materials, thermal regulation systems, and novel composite manufacturing

The enhanced heat transfer performance demonstrated in this study through the use of CuO-air nanofluids has direct and significant implications for the sustainable manufacturing of advanced building and structural materials. The Bridgman–Stockbarger method, while originally developed for high-purity crystal growth, shares fundamental thermal processing principles with several energy-intensive material production routes, including the sintering of advanced ceramics, the curing of polymer composites, and the solidification of phase-change materials used in building envelopes. The observed improvement in the average Nusselt number—up to 36% at Ra=10^6 and φ=0.05—translates directly into a reduction in thermal processing time and energy input. For instance, in the sintering of alumina or silicon carbide ceramics, furnace temperatures often exceed 1,600°C, and heating cycles can last several hours. A 20–30% enhancement in convective heat transfer could reduce cycle times by an estimated 15–25%, leading to proportional decreases in electrical or gas energy consumption. This aligns with global efforts to decarbonize industrial heating, which accounts for approximately 20% of total industrial energy use. Beyond energy savings, the improved temperature uniformity observed at higher aspect ratios and moderate nanoparticle concentrations (see Figure 2) is critical for minimizing thermal stresses and defects in manufactured components. In fiber-reinforced composite curing, uneven temperature distribution can lead to residual stresses, warping, or incomplete polymerization. The use of nanofluids as a heat transfer medium in such processes could enhance temperature control, reduce scrap rates, and improve mechanical performance of the final product. The integration of nanofluid-based thermal management also supports circular economy principles in material processing. For example, the production of cement and steel—two of the most carbon-intensive building materials—relies heavily on high-temperature furnaces. While this study focuses on annular geometries, the underlying heat transfer enhancement mechanisms are applicable to other furnace configurations. Reduced energy consumption per unit of material processed directly lowers greenhouse gas emissions. Furthermore, the potential to operate at lower peak temperatures or with shorter dwell times could extend furnace liner lifespans and reduce maintenance-related waste. For industrial adoption, several practical aspects must be considered:

(1) Nanofluid stability and cost: CuO nanoparticles are commercially available and relatively low-cost compared to

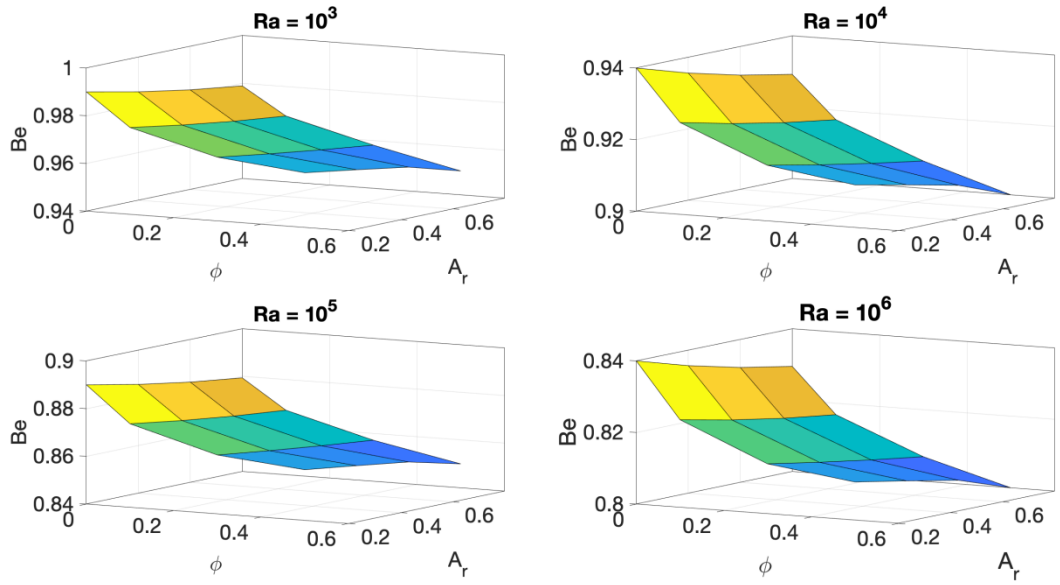


Figure 10. Bejan Number at Different Aspect Ratios, Rayleigh Numbers and Nanoparticle Concentrations.

noble metal nanoparticles. Stability can be maintained through surfactant addition or ultrasonication.

(2) System compatibility: Nanofluids can be integrated into existing furnace cooling/heating loops with minimal retrofit.

(3) Safety and handling: As noted in Section 1, exposure to airborne nanoparticles must be controlled via ventilation and personal protective equipment, following established NIOSH guidelines.

5 CONCLUSION

This study employed a Multi-Relaxation-Time Lattice Boltzmann Method (MRT-LBM) to investigate the natural convection heat transfer and entropy generation of CuO–air nanofluid within a vertical annular geometry, with direct applications to Bridgman–Stockbarger crystal growth furnaces and sustainable material processing. When it comes to heat transfer between coaxial cylinders, it's actually related to natural convection heat transfer in vertical cylindrical enclosures. As for the common method used for growing single crystals application, Bridgman-Stockbarger, they directly related which both involve heat transfer in engineering calculations. The objective of this study is to investigate the natural convection phenomenon using an advanced numerical approach. We utilize the MRT lattice Boltzmann method to simulate the flow behavior and heat transfer within a symmetrical cone. The working fluid employed is a CuO-air nanofluid, with its properties determined using state-of-the-art devices. The governing parameters in this investigation are the Rayleigh number, nanoparticle concentration, and aspect ratio of the cone. Our findings indicate that the addition of CuO nanoparticles to pure water enhances the heat transfer performance of the cavity. This is evidenced by an increase in the average Nusselt number at higher solid volume fractions of the nanofluid. Additionally, the Rayleigh number has a significant effect on the average Nusselt number, with the local fluid friction irreversibility and local heat transfer irreversibility being dominant near the active side wall. Furthermore, as the Rayleigh number and solid volume fraction of the nanofluid increase, the volumetric entropy generation also intensifies.

Key Findings are:

(1) The addition of CuO nanoparticles significantly enhances heat transfer performance, with the average Nusselt number increasing by up to 36% at $Ra=10^6$ and $\varphi=0.05$ compared to pure air.

(2) The aspect ratio (*AR*) and Rayleigh number (*Ra*) strongly influence flow structure and temperature uniformity. Higher *AR* promotes multi-cellular convection, while increased *Ra* intensifies buoyancy-driven flow and thermal gradients.

(3) Entropy generation analysis reveals a trade-off between thermal and viscous irreversibilities. While nanoparticle inclusion reduces thermal irreversibility due to improved conductivity, it increases fluid friction irreversibility owing to elevated viscosity.

(4) The Bejan number decreases with increasing *Ra* and φ, indicating a shift toward friction-dominated entropy production under stronger convection and higher nanoparticle loading.

The findings of this study demonstrate a significant enhancement in thermal management through the use of nanofluids within the Bridgman–Stockbarger furnace configuration, with direct implications for the field of building material science. The improved heat transfer efficiency and optimized temperature uniformity achieved via nanofluid integration can directly benefit the production of advanced construction materials such as high-performance ceramics, fiber-reinforced composites, and phase-

change materials used for thermal regulation in buildings. For instance, the reduction in energy consumption aligns with the growing demand for sustainable manufacturing practices in the construction industry, particularly in the processing of energy-intensive materials like cement and steel. Moreover, the observed decrease in entropy generation underscores the potential for minimizing thermodynamic waste, which is critical for enhancing the durability and lifecycle performance of building components. These results not only validate the application of nanofluids in crystal growth systems but also provide a scalable framework for improving thermal efficiency in other material processing operations relevant to building science, such as sintering, annealing, and solidification of recycled or non-traditional materials. Thus, this work contributes to the broader goals of Journal of Building Material Science by offering insights into energy-efficient, sustainable material processing technologies that can drive innovation in modern construction and engineering applications.

This work provides several original contributions to the field of nanofluid-enhanced thermal systems and sustainable material processing:

(1) First application of MRT-LBM to CuO–air nanofluid in a vertical annulus with coupled entropy generation analysis, offering detailed insights into both heat transfer enhancement and thermodynamic losses.

(2) Explicit linkage between nanofluid performance and sustainable building material manufacturing, demonstrating how heat transfer improvements can reduce energy consumption in ceramic sintering, composite curing, and phase-change material processing.

(3) Comprehensive parametric study integrating the effects of Ra*Ra*, φ*φ*, and AR*AR* on Nusselt number and entropy generation, providing design guidelines for optimizing furnace efficiency and material quality.

This study provides a numerical foundation for utilizing nanofluids to enhance thermal efficiency in material processing furnaces. The quantified improvements in heat transfer and entropy generation offer a pathway to:

(1) Reduce specific energy consumption in ceramic, composite, and phase-change material production.

(2) Enhance product quality through better thermal management.

(3) Support the development of next-generation, energy-efficient building materials such as ultra-high-performance concrete (UHPC), transparent ceramics, and smart thermal storage composites.

Future work should focus on experimental validation in pilot-scale furnaces and lifecycle assessment (LCA) to quantify net environmental benefits. To continue current study, one can calculate the local heat transfer between coaxial cylinders in the Bridgman-Stockbarger application with a spacewise heat flux, which can use established heat transfer equations and numerical methods here. As for the use of other nanoparticles in an experimental setting, researchers can explore the thermal conductivity enhancement and heat transfer effects of various nanoparticles in Bridgman-Stockbarger applications.

To build upon this numerical study, the following directions are recommended:

(1) Experimental validation using a lab-scale Bridgman–Stockbarger setup with CuO–air nanofluid to verify the predicted heat transfer and flow characteristics.

(2) Extension to other nanoparticle types (e.g., Al_2O_3, TiO_2, hybrid nanofluids) and base fluids (e.g., ethylene glycol, molten salts) to identify optimal compositions for specific material processing applications.

(3) Investigation of transient and phase-change effects in nanofluid-based systems, relevant to solidification processes in crystal growth and thermal energy storage.

(4) Lifecycle and techno-economic analysis to assess the environmental and economic viability of implementing nanofluid technology in industrial-scale material processing furnaces.

In summary, this study demonstrates that nanofluid integration can substantially improve the thermal efficiency and sustainability of high-temperature material processing systems. The findings offer a computational foundation for designing next-generation furnaces and thermal management systems aligned with green manufacturing and sustainable building material production.

Acknowledgements

Not applicable.

Conflicts of Interest

The authors declared no conflict of interest.

Data Availability

The datasets generated during and/or analyzed during the current study are available from the corresponding author on reasonable request.

Copyright Permissions
Copyright © 2026 The Author(s). Published by Innovation Forever Publishing Group Limited. This open-access article is licensed under a Creative Commons Attribution 4.0 International License (https://creativecommons.org/licenses/by/4.0), which permits unrestricted use, sharing, adaptation, distribution, and reproduction in any medium, provided the original work is properly cited.

Author Contribution
study conception and design; data collection; analysis and interpretation of results; draft manuscript preparation is performed by Jamalabadi MYA. The author reviewed the results and approved the final version of the manuscript.

References
[1] Bridgman PW. Certain physical properties of single crystals of tungsten, antimony, bismuth, tellurium, cadmium, zinc, and tin. *Proc Am Acad Arts Sci*, 1925; 60: 305-383.[DOI]
[2] Stockbarger DC. The production of large single crystals of lithium fluoride. *Rev Sci Instrum*, 1936; 7: 133-136.[DOI]
[3] Broadbent TAA. Investigations on the Theory of the Brownian Movement. By A. Einstein. Pp. 122. $1.25. 1956 – The Principles of Mechanics. By H. Hertz. Pp. xlii, 274. $1.75. 1956 – Hydrodynamics. By H. L. Dryden, F. P. Murnaghan and H. Bateman. Pp. 634. $2.50. 1956. (Dover Publications, New York). Math Gaz, 1957; 41: 231.[DOI]
[4] Hamilton R, Crosser O. Thermal Conductivity of Heterogeneous Two-Component Systems. *Ind Eng Chem Fundam*, 1962; 1: 187-191.[DOI]
[5] Levin MI, Miller MA. Maxwell's "Treatise on Electricity and Magnetism". *Usp Fiz Nauk*, 1981; 135: 425-455.[DOI]
[6] Kumar R, Kalam MA. Laminar thermal convection between vertical coaxial isothermal cylinders. *Int J Heat Mass Transf*, 1991; 34: 513-524.[DOI]
[7] Crawford L, Lemlich R. Natural convection in horizontal concentric cylindrical annuli. *Ind Eng Chem Fundam*, 1962; 1: 260-264.[DOI]
[8] Yu W, Choi SUS. The role of interfacial layers in the enhanced thermal conductivity of nanofluids: a renovated Hamilton–Crosser model. *J Nanopart Res*, 2004; 6: 355-361.[DOI]
[9] Li Q, He YL, Tang GH et al. Lattice Boltzmann model for axisymmetric thermal flows. *Phys Rev E*, 2009; 80: 037702.[DOI]
[10] Dahm MM, Yencken MS, Schubauer-Berigan MK. Exposure Control Strategies in the Carbonaceous Nanomaterial Industry. *J Occup Environ Med*, 2011; 53: S68-S73.[DOI]
[11] NIOSH. NIOSH Current Intelligence Bulletin: Occupational Exposure to Carbon Nanotubes and Nanofibers. DHHS (NIOSH) Publication, 2010.
[12] NIOSH. NIOSH Current Intelligence Bulletin 63: Occupational Exposure to Titanium Dioxide. DHHS (NIOSH) Publication No. 2011-160, 2011.
[13] Li L, Mei RW, Klausner JF. Multiple-relaxation-time lattice Boltzmann model for the axisymmetric convection diffusion equation. *Int J Heat Mass Transf*, 2013; 67: 338-351.[DOI]
[14] Mehel A, Murzyn F. Effect of air velocity on nanoparticles dispersion in the wake of a vehicle model: Wind tunnel experiments. *Atmos Pollut Res*, 2015; 6: 612-617.[DOI]
[15] Adebayo O, Salaudeen SA, Al-Farhany K et al. Modelling of Heat Transfer Characteristics around a Cylindrical-Barrier. *Int J Eng Model*, 2022; 35: 1-12.[DOI]
[16] Jamalabadi MYA. Lattice Boltzmann Simulation of Ferrofluids Film Boiling. *Processes*, 2020; 8: 881.[DOI]
[17] Sankar M, Reddy NK, Do Y. Conjugate buoyant convective transport of nanofluids in an enclosed annular geometry. *Sci Rep*, 2021; 11: 13141.[DOI]
[18] Swamy HAK, Reddy NK, Sankar M et al. Conjugate heat transfer of aqueous hybrid nanoliquid between coaxial cylinders subjected to magnetic field. *Int J Thermofluids*, 2023; 17: 100299.[DOI]
[19] Hayat T, Yazman M, Muhammad K et al. Radiative and dissipative flow of hybrid nanofluid between two coaxial cylinders: A comparative numerical study. *Alex Eng J*, 2023; 71: 79-88.[DOI]
[20] Alami AH, Ramadan M, Tawalbeh M et al. A critical insight on nanofluids for heat transfer enhancement. *Sci Rep*, 2023; 13: 15154.[DOI]
[21] Capper P, Rudolph P. Crystal Growth Technology. Wiley-VCH: Weinheim, Germany, 2010.[DOI]
[22] Hanif H, Ilias MR, Iqbal Z et al. Heat transfer in hybrid nanofluid flow between two coaxial cylinders. *Case Stud Therm Eng*, 2024; 53: 104327.[DOI]
[23] Venkatachalappa M, Sankar M, Natarajan AA. Natural convection in an annulus between two rotating vertical cylinders. *Acta Mech*, 2001; 147: 173-196.[DOI]
[24] Wang X, Wang QJ, Ren N et al. Lubrication subjected to effects of electric and magnetic fields: recent research progress and a generalized MEMT-field Reynolds equation. *Front Mech Eng*, 2024; 9: 1334814.[DOI]
[25] Li S, Raghunath K, Alfaleh A et al. Effects of activation energy and chemical reaction on unsteady MHD dissipative Darcy–Forchheimer squeezed flow of Casson fluid over horizontal channel. *Sci Rep*, 2023; 13: 2666.[DOI]
[26] Kondakrindi K, Reddigari MR, Koniredy H et al. Nanofluids (CuO & TiO2) - water as heat transfer fluid in a thermal energy storage

system for applications of solar heating: An experimental study. *Therm Sci*, 2023; 27: 4375-4388.[DOI]

[27] Behzadnia A, Moosavi-Nasab M, Oliyaei N. Anti-biofilm activity of marine algae-derived bioactive compounds. *Front Microbiol*, 2024; 15: 1270174.[DOI]

[28] Arshad M, Hussain A, Hassan A et al. Thermal energy investigation of magneto-hydrodynamic nano-material liquid flow over a stretching sheet: comparison of single and composite particles. *Alex Eng J*, 2022; 61: 10453-10462.[DOI]

[29] Jamalabadi MYA. Use of Nanoparticle Enhanced Phase Change Material for Cooling of Surface Acoustic Wave Sensor. *Fluids*, 2021; 6: 31.[DOI]

[30] Jamalabadi MYA. Feasibility Study of Cooling a Bulk Acoustic Wave Resonator by Nanoparticle Enhanced Phase Change Material. *Magnetochemistry*, 2021; 7: 144.[DOI]

[31] Jamalabadi MYA. Joule heating in low-voltage electroosmotic with electrolyte containing nano-bubble mixtures through microchannel rectangular orifice. *Chem Eng Res Des*, 2015; 102: 407-415.[DOI]

[32] Jamalabadi MYA. Optimal Design of Free Convection in an Elliptical Annulus Using Al2O3 Ethylene Glycol Nanofluid. *J Nano Res*, 2025; 14: 478-491.[DOI]

[33] Ahmed N, Khan UA, Mohyud-Din ST. Influence of viscous dissipation on a copper oxide nanofluid in an oblique channel: implementation of the KKL model. Eur Phys J Plus, 2017; 132: 176.[DOI]

[34] Ehsan MA, Awan SE, Raja MAZ et al. Heat transfer in nanomaterial suspension (CuO and Al_2O_3) using KKL model. Coatings, 2021; 11: 417.[DOI]